ACADEMIC PRESS

Available online at www.sciencedirect.com

SCIENCE DIRECT®

Journal of Computational Physics 184 (2003) 592–618

JOURNAL OF COMPUTATIONAL PHYSICS

www.elsevier.com/locate/jcp

A spectral Chebyshev method for linear stability analysis of one-dimensional exact solutions of gas dynamics

Carine Boudesocque-Dubois, Jean-Marie Clarisse, Serge Gauthier *

CEA Bruyères le Châtel, B.P.12, 91680-Bruyères le Châtel, France

Received 16 January 2002; received in revised form 19 September 2002; accepted 21 October 2002

Abstract

We present a spectral numerical method for solving one-dimensional systems of partial differential equations (PDEs) which arise from linearization of the Euler equations about an exact solution depending on space and time. A two-domain Chebyshev collocation method is used. Matching of quantities is performed in the space of characteristic variables as suggested by Kopriva [Appl. Numer. Math. 2 (1986) 221; J. Comput. Phys. 125 (1996) 244]. Time-dependent boundary conditions are handled following an approach proposed by Thompson [J. Comput. Phys. 68 (1987) 1; 89 (1990) 439]. An exact numerical stability analysis valid for any explicit three-step third-order non-degenerate Runge–Kutta scheme is provided. The numerical method is tested against exact solutions for the three fundamental modes of a compressible flow (entropy, vorticity and acoustic modes).

Keywords: Spectral method; Gas dynamics; Stability analysis

1. Introduction

In this paper we present a numerical method for solving systems of partial differential equations (PDEs) which arise from linearization of the Euler equations about a one-dimensional exact solution depending on space and time.

Stability analyses of fluid flows often start with a linear stability analysis. In situations where the mean flow depends on time, linearizing the Euler or the Navier–Stokes equations about such a flow leads to a linear system of PDEs for perturbations. The coefficients of this linear system depending on space and time variables, the normal mode analysis [3] no longer applies and one has to solve an

* Corresponding author. Tel.: +33-1-4595-6810; fax: +33-1-4386-7429.
E-mail addresses: carine.boudesocque@cea.fr (C. Boudesocque-Dubois), jean-marie.clarisse@cea.fr (J.-M. Clarisse), serge.gauthier@cea.fr (S. Gauthier).

0021-9991/02/$ - see front matter
PII: S0021-9991(02)00039-6

initial and boundary value problem (IBVP) for the perturbations. The one-dimensional exact solutions that are considered here are of self-similar types [30]. Most of the time, the set of ordinary differential equations (ODEs) resulting from the self-similar analysis must be solved numerically.

The linear stability of exact solutions of the Euler equations has been addressed by several authors [1,17,20,25,28,29]. In these examples, the mean flows are obtained from analytical calculations. Moreover, the linear perturbation analysis can also be carried out analytically [1,17,25,28]. More generally, some extra assumptions (considering only solenoidal perturbations, for example) may be needed to analytically solve the linear IBVP [1]. Sometimes, even when the exact solution is known explicitly, the linear IBVP is solved numerically [29]. In situations where the mean flow is only known numerically, the linear IBVP must also be solved numerically (see e.g. [24]). The linear system of PDEs entering in this IBVP is of hyperbolic type and exhibits a specific structure. Indeed the linear stability analysis of such one-dimensional solutions relies on a Fourier decomposition of the transverse motion perturbations. As a result, the linear system of PDEs depends explicitly on the transverse wavenumber.

Numerical integrations of such IBVPs with finite difference methods have been previously carried out: see for example [29]. On the other hand, spectral methods have been shown to be very efficient for numerically solving PDEs. This efficiency is due to the low requirement in terms of number of collocation points per wavelength since the convergence is generally faster than algebraic. This feature is especially desirable when one wishes to accurately describe acoustic waves as it is the case with the linearized Euler equations. In a more general context, multidomain solutions of the Euler and Navier–Stokes equations have been investigated, see [11–15,19].

Here we propose a collocation Chebyshev method for handling the above-mentioned particular form of the linearized Euler equations. The algorithm is based on an explicit three-step third-order Runge–Kutta scheme, a treatment of time-dependent boundary conditions according to Thompson's approach [22,23], and a matching of quantities at subdomain interfaces following Kopriva's work [10,15]. The numerical stability analysis of this algorithm is derived explicitly for periodic and Dirichlet boundary conditions in the case of uniform and constant mean flows. From this study, it turns out that the stability constraint on the timestep depends strongly on the transverse wavenumber.

We have in mind applications to stability analyses of self-similar solutions of a particular form. An example of such applications is the problem of the hydrodynamic stability of a centered rarefaction wave: see [25]. In this specific case, provided that proper boundary conditions are specified, the mean flow is a non-uniform, non-constant self-similar exact solution of the Euler equations. This paper addresses some of the numerical difficulties encountered when applying the present method to such cases.

The outline of the paper is the following: the linear perturbation equations are detailed in the general case in Sections 2, Section 3 describes the numerical method, Section 4 deals with the numerical stability analysis, and finally results of test cases are reported in Section 5.

2. Equations and boundary conditions

2.1. Mean flow equations

Consider the motion of an inviscid, non-heat-conducting fluid, obeying the polytropic equation of state. The equations of motion – the three-dimensional Euler equations – can be written, in Eulerian form and Cartesian coordinates (x, y, z), as

$$\begin{aligned}
&\frac{\partial \rho}{\partial t} + \vec{v}\cdot\nabla\rho + \rho\nabla\cdot\vec{v} = 0,\\
&\rho\left(\frac{\partial \vec{v}}{\partial t} + \vec{v}\cdot\nabla\vec{v}\right) + \nabla p = \vec{0},\\
&\frac{\partial p}{\partial t} + \vec{v}\cdot\nabla p + \gamma p\nabla\cdot\vec{v} = 0,
\end{aligned} \tag{1}$$

where ρ, the fluid density, $\vec{v} = v_x\vec{e}_x + v_y\vec{e}_y + v_z\vec{e}_z$, the fluid velocity vector, p, the fluid pressure, depend on the coordinate vector $\vec{x} = (x, y, z)$ and t, and γ is the fluid adiabatic exponent.

For one-dimensional motions in the x-direction, we denote by $\bar{x}, \bar{\rho}, \bar{v}_x, \bar{p}$, the corresponding fluid quantities. Introducing the Lagrangian coordinate m defined by the equation

$$m = \int_{\bar{x}(0,t)}^{\bar{x}(m,t)} \bar{\rho}(x,t)\mathrm{d}x, \tag{2}$$

the equations of motion (1) can be written, in Lagrangian form, as the one-dimensional system

$$\begin{aligned}
&\frac{\partial \bar{\rho}}{\partial t} + \bar{\rho}^2\frac{\partial \bar{v}_x}{\partial m} = 0,\\
&\frac{\partial \bar{v}_x}{\partial t} + \frac{\partial \bar{p}}{\partial m} = 0,\\
&\bar{v}_y = \bar{v}_z = 0,\\
&\frac{\partial \bar{p}}{\partial t} + \gamma\bar{\rho}\bar{p}\frac{\partial \bar{v}_x}{\partial m} = 0,
\end{aligned} \tag{3}$$

where now $\bar{\rho}$, $\bar{v}_x(= \partial\bar{x}/\partial t)$ and $\bar{p}$ are taken as functions of (m, t). This system constitutes the mean flow equations of motion.

2.1.1. Particular cases of self-similar solutions

Our primary motivation lies in linear stability analyses of self-similar solutions of (3) having the form

$$\bar{\rho}(m,t) = \varrho\bar{G}(\xi), \quad \bar{v}_x(m,t) = \frac{A}{\varrho}t^{\alpha-1}\bar{V}(\xi), \quad \bar{p}(m,t) = \frac{A^2}{\varrho}t^{2(\alpha-1)}\bar{P}(\xi), \tag{4}$$

where the similarity variable ξ is given by

$$\xi = \frac{m}{At^\alpha}, \tag{5}$$

the similarity exponent α being a real constant. Both ϱ and A are constants chosen so that the reduced functions $\bar{G}, \bar{V}, \bar{P}$ and the similarity variable ξ are dimensionless ([30], Chapter xii). This specific form covers many self-similar solutions of the one-dimensional gas dynamic equations [4,30]: e.g. centered rarefaction waves, shock waves, and Riemann problem solutions.

Introducing the reduced functions in (3) leads to a first-order ODE in the variable ξ for the unknown $\bar{\mathbf{V}} = (\bar{G} \quad \bar{V} \quad \bar{P})^\mathsf{T}$. The change of variables $(m, t) \to \xi$ transforms then any initial or boundary conditions supplementing the system of PDEs (3) into boundary conditions at fixed ξ-abscissas (eventually infinite) for the ODE satisfied by $\bar{\mathbf{V}}$. In particular, any discontinuity – contact discontinuity or wave front – of a

solution $\bar{\mathbf{V}}$ is, due to the self-similar assumption, of constant abscissa ξ. In that respect, choosing a Lagrangian form for the equations of motion (3), and the definition (5) for the similarity variable ξ is justified by the fact that it greatly simplifies the handling of contact discontinuities. Performing linear stability analyses of such self-similar solutions requires of course that these solutions are known – either explicitly or numerically – including the locations of their discontinuities, if any.

2.1.2. Restriction to uniform and constant mean flows

Prior to considering stability analyses of solutions of the type (4), this paper focuses on the case of uniform and constant mean flows. The reason for doing so is twofold. First, such a restriction will allow us to formulate explicit numerical stability criteria which will be of practical use, in more general cases, for the numerical method we propose. Second, we will be able to provide quantitative results regarding the stability and accuracy of this method thanks to the availability of exact solutions in this simplified setting. The assumption of uniform and constant flows implies that the reduced functions in (4) are independent of the variable ξ since the corresponding functions of (m,t) are constant. With the exception of Section 2.2 and of Appendix A, the rest of this paper relies on this simplifying assumption.

In addition, in order to avoid unnecessary complications brought by the self-similar transformation (4) and (5), we have retained, for the sequel, formulations of the motion equations in the variables (m,t) rather than in the variables (ξ,t). This choice is justified by the fact that the change of variables $(m,t) \to (\xi,t)$ does not alter the properties of the linear perturbation equations: see Section 2.2 and Appendix A. Consequently the remarks made in the preceding paragraph regarding the locations of boundary conditions and discontinuities of the self-similar solutions $\bar{\mathbf{V}}$ must be transposed – however unrealistic this may seem – to the corresponding functions of (m,t): i.e., $\bar{\rho}$, $\bar{v}_x$, and $\bar{p}$. We emphasize that this peculiarity is a pure matter of convenience and is without consequence for both the numerical stability results of Section 4 and the numerical method implementation which actually relies on (ξ,t)-formulations.

2.2. Linear perturbation equations

In fluid mechanics, one classically formulates the linear stability problem of a mean flow in terms of perturbations which, without further assumption, are functions of three space variables and time. These perturbations are sought as solutions of an IBVP given by: (a) a linearized form of the three-dimensional Euler equations 1, (b) linear perturbations of the boundary conditions satisfied by the mean flow under study, and (c) initial conditions.

Here, we have retained an Eulerian description of the perturbations in the coordinate system (m,y,z) for the formulation of this IBVP. This particular choice follows not only from the coordinate system used for the one-dimensional solution, but also from the fact that a Lagrangian description of the perturbations would further complicate the definition of initial conditions. Indeed, in the case of a Lagrangian description, initial position perturbations would have to be supplied in addition to the initial conditions required by an Eulerian description. As is usual, the formulation of this linear perturbation IBVP is simplified by performing a Fourier transform in the yz-plane – or *transverse* plane – of the linear perturbation equations and boundary conditions. Introducing the transverse wavenumber $k_\perp$ defined by

$$k_\perp = \sqrt{k_y^2 + k_z^2}, \tag{6}$$

the evolution equations for the linear perturbation Fourier components associated to $k_\perp$ may be written as (see Appendix A)

$$\frac{\partial \rho}{\partial t} + \bar{\rho}^2 \frac{\partial v_x}{\partial m} + \bar{\rho}\left(\frac{\partial \bar{v}_x}{\partial m}\rho + \frac{\partial \bar{\rho}}{\partial m} v_x + \nabla_\perp \cdot \vec{v}_\perp \right) = 0, \tag{7a}$$

$$\frac{\partial v_x}{\partial t} + \frac{\partial p}{\partial m} - \frac{1}{\bar{\rho}} \frac{\partial \bar{p}}{\partial m}\rho + \bar{\rho} \frac{\partial \bar{v}_x}{\partial m} v_x = 0, \tag{7b}$$

$$\frac{\partial}{\partial t}\left(\nabla_\perp \cdot \vec{v}_\perp \right) - \frac{k_\perp^2}{\bar{\rho}} p = 0, \tag{7c}$$

$$\frac{\partial p}{\partial t} + \gamma \bar{p}\left(\bar{\rho} \frac{\partial v_x}{\partial m} + \nabla_\perp \cdot \vec{v}_\perp \right) + \bar{\rho}\left(\frac{\partial \bar{p}}{\partial m} v_x + \gamma \frac{\partial \bar{v}_x}{\partial m} p \right) = 0, \tag{7d}$$

where now $\rho, v_x, \nabla_\perp \cdot \vec{v}_\perp, p$ denote the linear perturbation Fourier components of – respectively – the fluid density, the x-velocity, the transverse expansion, and the pressure, all taken as functions of $(m, k_\perp, t)$.

In writing down (7a)–(7d) we assume that the mean flow quantities $\bar{\rho}, \bar{v}_x, \bar{p}$ are sufficiently smooth for these PDEs to be meaningful in the class of $\mathscr{C}^n$-functions for some $n \geqslant 0$. Hence we consider the above system in regions excluding any discontinuity of the mean flow quantities or of their first order m-derivatives. Would the mean flow under study present such discontinuities, the corresponding linear perturbation jump conditions would be used to define boundary conditions for (7a)–(7d) as it is classically done in fluid mechanics. For practical applications, this approach is justified by the remarks made earlier (Section 2.1) about the mean flow boundary and discontinuity locations.

Eqs. (7a)–(7d) constitute a hyperbolic system of one-dimensional linear conservation laws with source terms. This system may be written, in terms of the vector of primitive variables $\mathbf{V} = (\rho \quad v_x \quad \nabla_\perp \cdot \vec{v}_\perp \quad p)^\mathsf{T}$, as

$$\frac{\partial \mathbf{V}}{\partial t} + \mathbf{A}\frac{\partial \mathbf{V}}{\partial m} + \mathbf{B}\mathbf{V} = \mathbf{0} \tag{8}$$

with

$$\mathbf{A} = \begin{pmatrix} 0 & \bar{\rho}^2 & 0 & 0 \\ 0 & 0 & 0 & 1 \\ 0 & 0 & 0 & 0 \\ 0 & (\bar{\rho}\bar{c})^2 & 0 & 0 \end{pmatrix}, \tag{9}$$

and, in the particular case of uniform mean flows,

$$\mathbf{B} = \begin{pmatrix} 0 & 0 & \bar{\rho} & 0 \\ 0 & 0 & 0 & 0 \\ 0 & 0 & 0 & -k_\perp^2/\bar{\rho} \\ 0 & 0 & \gamma\bar{p} & 0 \end{pmatrix}. \tag{10}$$

Hereinabove, $\bar{c}$ denotes the isentropic sound velocity of the mean flow. With this notation, the eigenvalues of $\mathbf{A}$ – taking into account their order of multiplicity – are

$$\Lambda^1 = -\bar{\rho}\bar{c}, \quad \Lambda^2 = \Lambda^3 = 0, \quad \Lambda^4 = \bar{\rho}\bar{c}, \tag{11}$$

while a basis of corresponding eigenvectors is given by

$$\mathbf{R}^1 = \begin{pmatrix} \frac{1}{\bar{c}^2} \\ -\frac{1}{\bar{\rho}\bar{c}} \\ 0 \\ 1 \end{pmatrix}, \quad \mathbf{R}^2 = \begin{pmatrix} 1 \\ 0 \\ 0 \\ 0 \end{pmatrix}, \quad \mathbf{R}^3 = \begin{pmatrix} 0 \\ 0 \\ 1 \\ 0 \end{pmatrix}, \quad \mathbf{R}^4 = \begin{pmatrix} \frac{1}{\bar{c}^2} \\ \frac{1}{\bar{\rho}\bar{c}} \\ 0 \\ 1 \end{pmatrix}. \tag{12}$$

Hence system (8) is hyperbolic, its eigenvalues being those of the linearized system of one-dimensional gas dynamics written in Lagrangian coordinates. We note however that since the transverse motion – in the form of its transverse expansion $\nabla_\perp \cdot \vec{v}_\perp$ – is incorporated in the vector of primitive variables $\mathbf{V}$, this system is nonstrictly hyperbolic, 0 being a double eigenvalue. We recall that a system of q equations of the form of (8) is said to be hyperbolic if the eigenvalues of the matrix $\mathbf{A}$ are all real and if the corresponding eigenvectors form a basis of $\mathbb{R}^q$. If in addition these eigenvalues are distinct, the system is called strictly hyperbolic: e.g. see [4]. For one-dimensional linear hyperbolic systems such as (8), the main consequence of nonstrict hyperbolicity is that characteristics may be surfaces or subspaces of higher dimensions, instead of curves.

For a uniform mean flow, some of the characteristic fields defined by (12) can be identified with the three basic fluctuation modes of a compressible flow [2]. Hence, the first (fourth) characteristic field corresponds to left- (respectively, right-) propagating acoustic plane waves along the x-direction with Lagrangian propagation velocity given by $\Lambda^1 = -\bar{\rho}\bar{c}$ (respectively, $\Lambda^4 = \bar{\rho}\bar{c}$). Similarly, the second characteristic field coincides with entropy modes. However, the third characteristic field only represents purely transverse dilatations and is not specifically associated with any of these basic modes. Further inspection of system (8) leads to the following remarks:

- For purely longitudinal perturbations, i.e., depending only on m and t, system (8) reduces to the linear one-dimensional system of gas dynamics in Lagrangian coordinates since then $k_\perp = 0$.
- For purely transverse perturbations, i.e., depending only on $k_\perp$ and t, system (8) degenerates into a system of first order ODEs.

Therefore, depending on the spatial dependence of the perturbations under consideration, the nature of the system of equations to be solved may change radically. This peculiarity has of course profound implications when considering the numerical approximation of (8). Note that all of the above remarks also apply to the (ξ, t)-formulation of the linear perturbation Eqs. (7a)–(7d) given in Eqs. (A.6)–(A.8) of Appendix A, hence justifying our choice of using formulations in the (m, t)-variables.

As previously stated, boundary conditions for the solutions of the linear system (8) result from a perturbation and linearization process applied to the mean flow boundary conditions. In this paper we do not address the problem of defining and implementing boundary conditions for this system of equations in its generality. Instead we focus on the numerical treatment of (i) periodic boundary conditions, (ii) non-reflecting boundary conditions, and (iii) time-dependent physical boundary conditions bearing on the density perturbations. In particular, the cases of material surface boundary conditions and of shock-wave jump relations are not considered here.

We note that the positions of the mean flow boundary conditions are stationary in the ξ- (alternatively m-) coordinate system (cf. Section 2.1). In addition, for the sake of simplicity, we assume here that the boundary conditions for the linear perturbations are applied at the same positions as those for the mean flow, i.e., at points of fixed ξ- (alternatively m-) abscissas. This assumption is fully compatible with the boundary conditions of types (i) and (ii) listed hereinabove, but restricts the kind of boundary conditions of type (iii) that can be handled. For example, boundary conditions at a material surface cannot be treated. Indeed, in such a case, a proper definition would include an evolution equation for the linear perturbation of the exact boundary location, a complication we do not wish to introduce for the moment.

3. Numerical method

Since system (8) is solved on a bounded domain, we need to address the way physical boundary conditions are handled. In this paper, we consider a two-domain method, in which case we also need to detail the way quantities are matched at the subdomain interface. Indeed, for an open flow, a proper control of wave reflections from and wave transmissions at boundaries is necessary. Accurate boundary condition

treatments are especially required for high-order numerical methods. In the following, we start by describing the boundary condition treatments for physical boundary conditions and matching conditions at the subdomain interface, and pursue by defining the numerical approximation method applied within each subdomain.

3.1. Boundary condition treatment

For a hyperbolic system of equations, it is known that given a set of physical conditions at a boundary, the number of boundary conditions required depends on the set of characteristics at this point [9]. When dealing with a linear hyperbolic system, as it is the case here, the method of characteristics provides an appropriate framework for the numerical treatment of boundary conditions [9]. Based on this method, Thompson [22,23] has proposed boundary condition treatments for handling time-dependent boundary conditions. Thompson's approach, which we choose to follow here, consists in rewriting system (8) under characteristic form, i.e.,

$$\left(\mathbf{R}^{-1}\frac{\partial \mathbf{V}}{\partial t}\right)+\mathbf{\Lambda}\left(\mathbf{R}^{-1}\frac{\partial \mathbf{V}}{\partial m}\right)+\mathbf{R}^{-1}\mathbf{B}\mathbf{R}(\mathbf{R}^{-1}\mathbf{V})=\mathbf{0}, \tag{13}$$

where $\mathbf{\Lambda}$ is the eigenmatrix defined by (11), or

$$\mathbf{\Lambda}=\mathbf{R}^{-1}\mathbf{A}\mathbf{R}=\operatorname{diag}\Big(-\bar{\rho}\bar{c},0,0,\bar{\rho}\bar{c}\Big), \tag{14}$$

and $\mathbf{R}$ is the right eigenvector matrix $\mathbf{R}=(\mathbf{R}^1\quad\mathbf{R}^2\quad\mathbf{R}^3\quad\mathbf{R}^4)$, its inverse being

$$\mathbf{R}^{-1}=\begin{pmatrix}0 & -\frac{1}{2}\bar{\rho}\bar{c} & 0 & \frac{1}{2}\\ 1 & 0 & 0 & -1/\bar{c}^2\\ 0 & 0 & 1 & 0\\ 0 & \frac{1}{2}\bar{\rho}\bar{c} & 0 & \frac{1}{2}\end{pmatrix}. \tag{15}$$

For a partial differential system, the number of boundary conditions at a given point is at most equal to the degree of the system of equations. For a linear hyperbolic system, the number of boundary conditions that must be applied at a given point depends on the sign of the eigenvalues of the diagonal matrix $\mathbf{\Lambda}$ at this point. It is convenient to write the diagonal matrix $\mathbf{\Lambda}$ as

$$\mathbf{\Lambda}=\mathbf{\Lambda}_{\text{in}}+\mathbf{\Lambda}_{\text{out}}, \tag{16}$$

where $\mathbf{\Lambda}_{\text{in}}$ contains the incoming wave eigenvalues and $\mathbf{\Lambda}_{\text{out}}$ the outgoing wave eigenvalues. The incoming wave eigenvalues are determined with respect to the outgoing normal vector defined at the boundary: they correspond to the characteristics entering the domain (see Fig. 1 for an example). Applying this decomposition and left-multiplying (13) by the matrix $\mathbf{R}$ leads to the following equation at the boundary:

$$\frac{\partial}{\partial t}\mathbf{V}+\mathbf{R}(\mathscr{L}+\mathscr{L}^*)+\mathbf{B}\mathbf{V}=0, \tag{17}$$

where the vector $\mathscr{L}+\mathscr{L}^*$ is a splitting of the term $\mathbf{\Lambda}\mathbf{R}^{-1}(\partial\mathbf{V}/\partial m)$. The non-zero components of the vector $\mathscr{L}$ correspond to outgoing waves and are given by

$$\mathscr{L}=\mathbf{\Lambda}_{\text{out}}\mathbf{R}^{-1}\frac{\partial \mathbf{V}}{\partial m}, \tag{18}$$

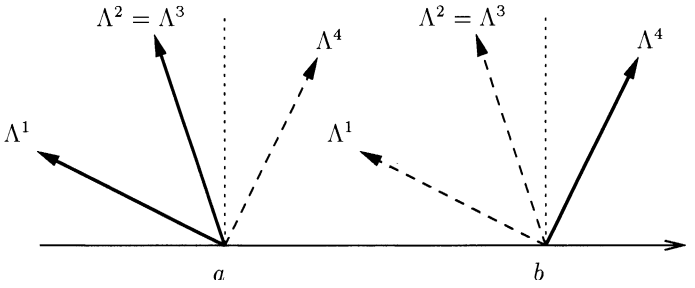

Fig. 1. Boundary condition treatment with the method of characteristics. Eigenvalues and definitions of the incoming (––) and outgoing (——) waves.

while the non-zero components of the vector $\mathscr{L}^*$ correspond to incoming waves, and are determined from the physical boundary conditions.

3.1.1. Periodic boundary conditions

For periodic boundary conditions on the domain $[m_0, m_1]$, the value of $\mathscr{L}^*$ at m_0 is defined by

$$\mathscr{L}^*(m_0) = \mathbf{\Lambda}_{\text{in}}\mathbf{R}^{-1}\left.\frac{\partial \mathbf{V}}{\partial m}\right|_{m_1^-}, \tag{19}$$

while its value at m_1 is

$$\mathscr{L}^*(m_1) = \mathbf{\Lambda}_{\text{in}}\mathbf{R}^{-1}\left.\frac{\partial \mathbf{V}}{\partial m}\right|_{m_0^+}. \tag{20}$$

The justification for this choice follows directly from the matching condition treatment detailed below (Section 3.2).

3.1.2. Non-reflecting boundary conditions

According to the characteristic variable analysis of Thompson [22,23], a non-reflecting boundary condition is characterized by the fact that the amplitudes of the incoming waves are constant, in time, at the boundary.

For purely longitudinal perturbations – i.e., such that $k_\perp = 0$ – system (8) reduces to the homogeneous linearized system of one-dimensional gas dynamics (Section 2.2) and can therefore be written in true characteristic form. Applying the above characterization of non-reflecting boundary conditions amounts then to taking $\mathscr{L}^* = 0$ in (17). This definition yields satisfactory results in numerical applications, even when the boundary is characteristic – i.e., coincides with one of the characteristics (see Section 5.4).

For non-zero transverse wavenumber ($k_\perp \neq 0$), the system of Eqs. (8) is no longer homogeneous due to the presence of the coupling term $\mathbf{BV}$. Consequently, this system cannot be written in true characteristic form. In particular, the equations in (13) are coupled. Nevertheless, following Thompson [23], one may still define $\mathscr{L}^*$ so that the amplitudes of the incoming wave components in (17), as identified by the decomposition (16), are constant in time. In effect, this corresponds to assigning the incoming wave components of $-\mathbf{R}^{-1}\mathbf{BV}$ to the non-zero components of $\mathscr{L}^*$. However, this definition has given poor results for configurations similar to the acoustic plane waves of Section 5.4, but with $k_\perp \neq 0$. Amplitudes of reflected waves which appeared at the non-reflecting boundary in these numerical experiments were sufficiently large to corrupt the whole resolution within a few periods of the exact solution. Moreover, results worsened with increasing values of $k_\perp$. This situation is reminiscent of numerical results observed with non-reflecting

boundary condition treatments based on the method of characteristics for the three-(two-)dimensional linearized Euler equations: see [21]. This is not surprising since system (8) can be viewed as the Fourier decomposition of these equations in the plane tangent to the boundary.

This defect of the characteristic based treatment is primarily due to the lack of a true characteristic formulation for the system of Eqs. (8) when $k_\perp \neq 0$. In these circumstances, the conditions to be imposed, at a boundary, on incoming and outgoing waves so as to eliminate reflected waves, are far from being clear. In addition, having to deal with boundaries which are characteristics of dimension $2 - m = \text{cst}$ corresponds to the second and third characteristic fields – does not simplify the matter. Consequently, we consider the present numerical treatment of non-reflecting boundary conditions to be applicable only for $k_\perp = 0$, although it has been used, with success, for non-propagative modes with $k_\perp \neq 0$ in some of the numerical tests of Section 5. We leave out, as an open question, the problem of a non-reflecting boundary condition numerical treatment compatible with the high accuracy of a Chebyshev spectral method.

3.1.3. Time-dependent boundary conditions

For time-dependent boundary conditions at abscissa m_0 or m_1, the number of flow variables to be prescribed corresponds to the number of incoming waves at this point. For example, at abscissa m_0, only one incoming wave is present so that a single boundary condition must be specified at this point. As a particular example, we choose to impose a time-dependent perturbed density ρ at m_0. Following Thompson [23], we define the value of the fourth component of $\mathscr{L}^*$ to be determined from the time-dependent condition

$$\rho(m = m_0, k_\perp, t) = \rho_0(t).$$

Combining this equation with the first equation of (17) gives the proper definition of $\mathscr{L}_4^*$, i.e.,

$$\mathscr{L}_4^* = -\mathscr{L}_1 - \bar{c}^2\left(\mathscr{L}_2 + (\mathbf{BV})_1 + \frac{\partial}{\partial t}\rho\right) = -\mathscr{L}_1 - \bar{c}^2\left(\mathscr{L}_2 + \bar{\rho}\nabla_\perp \cdot \vec{v}_\perp + \frac{\mathrm{d}}{\mathrm{d}t}\rho_0(t)\right). \tag{21}$$

The same reasoning applies when imposing any other flow quantities at any boundary point m_0.

3.2. Matching condition treatment

Matching the quantities at the subdomain interface is performed in a manner similar to the imposition of the physical boundary conditions. Indeed, the system of equations is solved on a subdomain with either physical boundary conditions or matching boundary conditions at each boundary. In the latter case, the non-zero components for incoming waves of the vector $\mathscr{L}^*$ are given by [10,15]

$$\mathscr{L}^* = \mathbf{\Lambda}_{\text{in}}\mathbf{R}^{-1}\left.\frac{\partial \mathbf{V}}{\partial m}\right|_{\text{neighbor}}, \tag{22}$$

where $\partial\mathbf{V}/\partial m|_{\text{neighbor}}$ means that the derivative is computed on the neighboring subdomain. This procedure amounts to introducing the proper upwinding at the boundary, as it is done, for example, in upwind finite difference methods.

3.3. Numerical approximation method

Given a spatial discretization of the domain $[a, b]$ by N points, the semi-discrete form of (8) is defined as

$$\frac{\partial}{\partial t}\mathbf{V}_{4N} + \mathbf{S}_{4N}\mathbf{V}_{4N} = 0, \tag{23}$$

where $\mathbf{V}_{4N}$ is a $4N$-component vector made of the N values of the density, followed by the N values of the x-velocity..., i.e.,

$$\mathbf{V}_{4N} = [\mathbf{V}_1(m_1)\cdots\mathbf{V}_1(m_N)\mathbf{V}_2(m_1)\cdots\mathbf{V}_3(m_N)\mathbf{V}_4(m_1)\cdots\mathbf{V}_4(m_N)]^{\mathsf{T}}.$$

In the above equation, $\mathbf{S}_{4N}$ is a $4N \times 4N$ operator, which depends only on the mean flow state, and is defined by

$$\mathbf{S}_{4N} = \mathbf{A}_{4N}\mathbf{D}_N^1\mathbf{I}_{4N} + \mathbf{B}_{4N}, \tag{24}$$

where

- $\mathbf{D}_N^1$ is the matrix of the first-order spatial derivative;
- $\mathbf{I}_{4N}$ the $4N \times 4N$ identity matrix;
- $\mathbf{A}_{4N}$ and $\mathbf{B}_{4N}$ are deduced from $\mathbf{A}$ and $\mathbf{B}$ (9), (10) in the same manner as the vector $\mathbf{V}_{4N}$ is deduced from $\mathbf{V}$.

At this point, we emphasize that the approximation of the first-order operator $\mathbf{D}_N^1$ is not yet specified. Several types of approximation may be used: finite differences or spectral methods. In this paper, we choose a collocation spectral method [18]. In this case, variables are expanded over a Chebyshev polynomial basis as

$$\mathbf{V}_{4N}(m) = \sum_{n=1}^{N} a_n T_n(x(m)), \tag{25}$$

with Gauss–Lobatto collocation points $x_i = \cos(i-1)\pi/(N-1)$, $i = 1,\ldots,N$, with the scaling $m(x) = (b-a)x/2 + (b+a)/2$. Spatial differentiation is then performed in the physical space by means of a matrix vector product.

The time discretization is defined with

$$t_{q+1} = t_q + \Delta t_q, \quad \Delta t_q > 0, \ q \in \mathbb{N},$$

and $\mathbf{V}^{(q)}$ denotes the value of the vector $\mathbf{V}$ at time t_q. In practice, an explicit three-step third-order Runge–Kutta scheme ([27], Eq. (11)) is used to perform the time integration.

4. Numerical stability analysis

As already stated, system (8) is a linearization of the one-dimensional gas dynamic equations. In this formulation, the transverse directions y and z have been Fourier-decomposed and reduced to the presence of the transverse wavenumber $k_\perp = \sqrt{k_y^2 + k_z^2}$. The resulting discretized system (23) inherits the same peculiarities as those of system (8) (see end of Section 2.2). Consequently the numerical stability properties of (23) are strongly affected by the transverse wavenumber $k_\perp$, as opposed to the purely one-dimensional case ($k_\perp = 0$) which has already been treated for Chebyshev collocation methods by Gottlieb [5,7]. In this section we derive rigorously numerical stability constraints within the von Neumann stability analysis [9] in the case of a uniform mean motion over a single computational domain.

System (23) being time integrated with a three-step third-order non-degenerate Runge–Kutta scheme, it follows that ([27], Section 7)

$$\mathbf{V}_{4N}^{(q+1)} = \left(\mathbf{I}_{4N} - \Delta t\mathbf{S}_{4N} + \frac{1}{2}(\Delta t\mathbf{S}_{4N})^2 - \frac{1}{6}(\Delta t\mathbf{S}_{4N})^3\right)\mathbf{V}_{4N}^{(q)} \equiv \mathbf{K}_{4N}(\Delta t)\mathbf{V}_{4N}^{(q)}. \tag{26}$$

A sufficient condition for strong stability of (26) is ([6], Chapter 9)

$$R(\mathbf{K}_{4N}(\Delta t)) = \max_{\lambda_{\mathbf{K}}} |\lambda_{\mathbf{K}}| \leqslant \|\mathbf{K}_{4N}(\Delta t)\| \leqslant 1 + \kappa\Delta t, \tag{27}$$

where R and $\lambda_{\mathbf{K}}$ are, respectively, the spectral radius and the eigenvalues of the amplification matrix $\mathbf{K}_{4N}(\Delta t)$, κ is a finite positive constant, and $\|\cdot\|$ is the Euclidean norm [26]. However, stability conditions involving only eigenvalues are, in practice, more convenient to use than the above condition. This leads us to consider the von Neumann condition, or

$$R(\mathbf{K}_{4N}(\Delta t)) \leqslant 1 + \kappa\Delta t,$$

which only provides a necessary condition for stability. Therefore, we adopt the more restrictive condition [9]

$$R(\mathbf{K}_{4N}(\Delta t)) \leqslant 1. \tag{28}$$

This condition corresponds, for any explicit three-step third-order non-degenerate Runge–Kutta scheme, to the inequality

$$\left|1 - \lambda\Delta t + \frac{1}{2}(\lambda\Delta t)^2 - \frac{1}{6}(\lambda\Delta t)^3\right|^2 \leqslant 1, \tag{29}$$

for all the eigenvalues λ of $\mathbf{S}_{4N}$. Therefore, in order to obtain a practical stability criterion, we first need to derive expressions for these eigenvalues.

4.1. Eigenvalues of the matrix $\boldsymbol{S}_{4N}$

The eigenvalues λ of the matrix $\mathbf{S}_{4N}$ being the roots of its characteristic polynomial, we have

$$\det(\mathbf{S}_{4N} - \lambda\mathbf{I}_{4N}) = \begin{vmatrix} -\lambda\mathbf{I}_N & \bar{\rho}^2\mathbf{D}_N^1 & \bar{\rho}\mathbf{I}_N & 0 \\ 0 & -\lambda\mathbf{I}_N & 0 & \mathbf{D}_N^1 \\ 0 & 0 & -\lambda\mathbf{I}_N & -(k_\perp^2/\bar{\rho})\mathbf{I}_N \\ 0 & (\bar{\rho}\bar{c})^2\mathbf{D}_N^1 & \bar{\rho}\bar{c}^2\mathbf{I}_N & -\lambda\mathbf{I}_N \end{vmatrix} = 0. \tag{30}$$

The above determinant may be first expanded with respect to the first block-column, since the first block-element is diagonal. The resulting $3N \times 3N$ determinant may be simplified by combining the second and third block-rows, and then expanded with respect to the second block-column. Hence (30) is replaced by

$$(-\lambda)^{2N} \begin{vmatrix} -\lambda\mathbf{I}_N & \mathbf{D}_N^1 \\ (\bar{\rho}\bar{c})^2\mathbf{D}_N^1 & -\frac{1}{\lambda}\left(\lambda^2 + k_\perp^2\bar{c}^2\right)\mathbf{I}_N \end{vmatrix} = (-\lambda)^{2N}\det(\mathbf{S}_{2N}) = 0. \tag{31}$$

Having noted that the blocks off the diagonal are identical up to a scalar coefficient and provided $\mathbf{D}_N^1$ can be put in diagonal form, we introduce $\mathbf{P}$, the left eigenvector matrix of $\mathbf{D}_N^1$, such that $\mathbf{D}_N^1 = \mathbf{P}^{-1}\,\mathrm{diag}(d_j)\mathbf{P}$, where d_j are the complex eigenvalues of $\mathbf{D}_N^1$. Then, by defining $\mathbf{J}_{2N}$ to be

$$\mathbf{J}_{2N} = \begin{pmatrix} 0 & \mathbf{P} \\ \mathbf{P} & 0 \end{pmatrix}, \tag{32}$$

the matrix $\mathbf{J}_{2N}^{-1}\mathbf{S}_{2N}\mathbf{J}_{2N}$ is block-diagonal of the form of Eq. (B.1), Appendix B. The characteristic polynomial of such a matrix comes as (Theorem B.1, Appendix B)

$$\prod_{j=1}^{N}\left(\lambda^2 + \bar{c}^2(k_\perp^2 - \bar{\rho}^2 d_j^2)\right). \tag{33}$$

Hence from (31), it turns out that Eq. (30) writes

$$(-\lambda)^{2N}\prod_{j=1}^{N}\left(\lambda^2+\bar{c}^2(k_\perp^2-\bar{\rho}^2d_j^2)\right)=0. \tag{34}$$

For the stability analysis, we need to fully characterize the spectrum of $\mathbf{S}_{4N}$. This requires us to determine the real and imaginary parts of the eigenvalues λ, which in turn depend on the real and imaginary parts of the eigenvalues d_j. Consequently we rewrite the non-zero roots of Eq. (34) as

$$(\mathrm{Re}[\lambda_j]+\mathrm{i}\mathrm{Im}[\lambda_j])^2=-\bar{c}^2\left(k_\perp^2-\bar{\rho}^2\left(\mathrm{Re}[d_j]^2-\mathrm{Im}[d_j]^2+2\mathrm{i}\mathrm{Re}[d_j]\,\mathrm{Im}[d_j]\right)\right),\quad j=1,\ldots,N. \tag{35}$$

This formulation allows us to obtain the following expressions for the eigenvalues λ_j:

- If $\mathrm{Re}(d_j)=0$,

$$\lambda_j=\pm\mathrm{i}\bar{c}\sqrt{\bar{\rho}^2\,\mathrm{Im}(d_j)^2+k_\perp^2}. \tag{36a}$$

- If $\mathrm{Im}(d_j)=0$ and $\bar{\rho}^2\,\mathrm{Re}(d_j)^2\geqslant k_\perp^2$,

$$\lambda_j=\pm\bar{c}\sqrt{\bar{\rho}^2\,\mathrm{Re}(d_j)^2-k_\perp^2}. \tag{36b}$$

- If $\mathrm{Im}(d_j)=0$ and $\bar{\rho}^2\,\mathrm{Re}(d_j)^2\leqslant k_\perp^2$,

$$\lambda_j=\pm\mathrm{i}\bar{c}\sqrt{k_\perp^2-\bar{\rho}^2\,\mathrm{Re}(d_j)^2}. \tag{36c}$$

- Otherwise

$$\lambda_j=\pm\frac{\bar{c}}{\sqrt{2}}\sqrt{\mathscr{Q}_j+\mathscr{R}_j}\left(\frac{1}{2\bar{\rho}^2}\frac{\mathscr{Q}_j-\mathscr{R}_j}{\mathrm{Re}(d_j)\,\mathrm{Im}(d_j)}-\mathrm{i}\right) \tag{36d}$$

with

$$\mathscr{Q}_j=k_\perp^2-\bar{\rho}^2\left(\mathrm{Re}(d_j)^2-\mathrm{Im}(d_j)^2\right),$$
$$\mathscr{R}_j=\sqrt{\left(2\bar{\rho}^2\,\mathrm{Re}(d_j)\,\mathrm{Im}(d_j)\right)^2+\mathscr{Q}_j^2}.$$

In all cases, the modulus of the eigenvalue is given by $|\lambda_j|=\bar{c}\sqrt{\mathscr{R}_j}$. We note that these expressions do not depend on the choice made for the first-order spatial derivative operator $\mathbf{D}_N^1$.

Having determined the eigenvalues of $\mathbf{S}_{4N}$, we may now turn to the formulation of the stability condition (29).

4.2. Numerical stability condition

The stability condition (29) defines a domain of stability in the plane $(X,Y)=(-\Delta t\,\mathrm{Re}(\lambda),-\Delta t\,\mathrm{Im}(\lambda))$: cf. [18, Fig. 4.16]. Given the shape of this domain, we consider the region defined by

$$\left(\frac{X}{\beta_1}\right)^2+\left(\frac{Y}{\beta_2}\right)^2\leqslant 1,\quad X\leqslant 0, \tag{37}$$

where

$$\beta_1 = 1 - \left(4+\sqrt{17}\right)^{-1/3} + \left(4+\sqrt{17}\right)^{1/3},$$
$$\beta_2 = \sqrt{3}.$$

The values of these coefficients correspond to the intersections of the stability domain boundary with the X- and Y-axes [18, Table 4.8]. One can check that the portion of elliptical region defined by (37) is contained in the domain of stability given by (29). This definition presents the advantage of being simpler to use than the stability region definition (29).

Given that $\mathrm{Re}(\lambda)$ and $\mathrm{Im}(\lambda)$ are expressed (Eqs. (36a)–(36d)) in terms of the eigenvalues d_j of the spatial operator $\mathbf{D}_N^1$, we now proceed to derive upper bounds $\widehat{\mathbf{Re}(\lambda)}$ and $\widehat{\mathbf{Im}(\lambda)}$ for the quantities $|\mathrm{Re}(\lambda)|$ and $|\mathrm{Im}(\lambda)|$. From the expressions (36a)–(36d), it appears that, in all cases, we have

$$\left.\begin{matrix}|\mathrm{Re}(\lambda)| \\ |\mathrm{Im}(\lambda)|\end{matrix}\right\} \leqslant \frac{\bar{c}}{\sqrt{2}}\sqrt{|\mathscr{Q}_j| + \mathscr{R}_j}. \tag{38}$$

An upper bound for $|\mathscr{Q}_j|$ is given by

$$|\mathscr{Q}_j| \leqslant k_\perp^2 + \bar{\rho}^2 \max\left(\widehat{\mathbf{Re}(d)}^2, \widehat{\mathbf{Im}(d)}^2\right), \tag{39}$$

where

$$\widehat{\mathbf{Re}(d)} = \max_j |\mathrm{Re}(d_j)|, \quad \widehat{\mathbf{Im}(d)} = \max_j |\mathrm{Im}(d_j)|. \tag{40}$$

From the definition of $\mathscr{R}_j$, we have

$$|\mathscr{R}_j| \leqslant |\mathscr{Q}_j| + 2\bar{\rho}^2\, \widehat{\mathbf{Re}(d)}\, \widehat{\mathbf{Im}(d)}. \tag{41}$$

From (38), (39), and (41), we define the upper bounds $\widehat{\mathbf{Re}(\lambda)}$ and $\widehat{\mathbf{Im}(\lambda)}$ to be

$$\widehat{\mathbf{Re}(\lambda)} = \widehat{\mathbf{Im}(\lambda)} = \bar{\rho}\bar{c}\sqrt{\left(\frac{k_\perp}{\bar{\rho}}\right)^2 + \max\left(\widehat{\mathbf{Re}(d)}^2, \widehat{\mathbf{Im}(d)}^2\right) + \widehat{\mathbf{Re}(d)}\, \widehat{\mathbf{Im}(d)}}. \tag{42}$$

At this point, the timestep constraint defined by (37) with (42) holds for several types of spatial approximation method: e.g. finite differences or spectral methods provided that $\mathbf{D}_N^1$ can be put in diagonal form. Note also that in practice, this constraint guarantees that the numerical scheme is used within the domain of stability defined by (29).

We now use this result for the Chebyshev collocation spectral method of Section 3.3. This requires us to determine the behaviors of the upper bounds $\widehat{\mathbf{Re}(d)}$ and $\widehat{\mathbf{Im}(d)}$ introduced in (40). As is well known [18], the modulus of the largest d_j is proportional to $(N-1)^2$, where N is the number of collocation points. However, we need to establish the asymptotic behavior of $\widehat{\mathbf{Re}(d)}$ and $\widehat{\mathbf{Im}(d)}$ as $N \to \infty$. These behaviors, listed in Table 1, have been checked numerically. Using these behaviors in (42), we obtain approximations

Table 1
Asymptotic growth of the modulus, the real and the imaginary parts of first-order derivative eigenvalues, computed on the domain $[-1,1]$

	$\frac{\max_{j=1,N}\lvert d_j\rvert}{(N-1)^2}$	$\beta_R = \frac{\max_{j=1,N}\lvert\mathrm{Re}(d_j)\rvert}{(N-1)^2}$	$\beta_I = \frac{\max_{j=1,N}\lvert\mathrm{Im}(d_j)\rvert}{(N-1)^2}$
Periodic boundary condition	0.218	0.000	0.218
Dirichlet boundary condition	0.089	0.022	0.086

for $\widehat{\mathbf{Re}(\lambda)}$ and $\widehat{\mathbf{Im}(\lambda)}$ as functions of $N, k_\perp$ and the computational domain length $(b-a)$. Given these approximations, we define a critical timestep Δt_c from (37), as

$$\Delta t_c = \frac{1}{\sqrt{\left(\frac{\widehat{\mathbf{Re}(\lambda)}}{\beta_1}\right)^2 + \left(\frac{\widehat{\mathbf{Im}(\lambda)}}{\beta_2}\right)^2}}, \tag{43}$$

and replace (37) by the condition $\Delta t \leqslant \Delta t_c$. We may then express explicitly the critical timestep for the two types of boundary conditions considered here. For a single domain $[a, b]$ and periodic boundary conditions– in which case λ is purely imaginary – one obtains

$$\Delta t_c = \frac{\sqrt{3}}{\bar{\rho}\bar{c}} \frac{b-a}{2(N-1)^2} \left[\left(\frac{k_\perp}{\bar{\rho}} \frac{b-a}{2(N-1)^2} \right)^2 + \beta_I^2 \right]^{-1/2}. \tag{44}$$

For Dirichlet boundary conditions, one gets

$$\Delta t_c = \frac{|\beta_1 \beta_2|}{\sqrt{\beta_1^2 + \beta_2^2}} \frac{b-a}{2(N-1)^2} \frac{1}{\bar{\rho}\bar{c}} \left[\left(\frac{k_\perp}{\bar{\rho}} \frac{b-a}{2(N-1)^2} \right)^2 + \max\left(\beta_R^2, \beta_I^2\right) + \beta_R \beta_I \right]^{-1/2}. \tag{45}$$

For a multidomain resolution, the smallest of the critical timestep values (44) or (45) over the subdomains is retained. The fact that this determination of Δt_c suffices for the scheme to be stable has been confirmed by investigating the maximum timestep values for stability in a series of numerical computations performed for different domain decompositions, numbers of collocation points, and transverse wavenumbers. The corresponding results, summarized in Table 3, are discussed in details in Section 5.2.

5. Numerical tests

The numerical method, detailed in Section 3, is tested against the three basic fluctuation modes of a compressible flow [2]: i.e., the entropy, vorticity and acoustic modes. For these tests, we consider numerical solutions of system (8) in the particular case of a uniform mean flow. More precisely, the mean motion is given by

$$\begin{pmatrix} \bar{\rho} & \bar{v}_x & \bar{p} \end{pmatrix}^{\mathsf{T}} = (4 \quad 0 \quad 4/3)^{\mathsf{T}}, \tag{46}$$

for a fluid adiabatic exponent $\gamma = 5/3$. Unless otherwise stated, computations are carried out on the domain $[0, 1]$, divided into two subdomains $[0, 0.5]$ and $[0.5, 1]$. All numerical results are obtained with a 15 significant digit floating point representation.

Table 2
Acoustic plane waves of arbitrary wavenumbers: wavenumber influence over the critical timestep, in the case of 2×40 collocation points, with periodic boundary conditions

$k_\perp$	1	10	10^2	10^3	10^4	10^5	10^7
Δt_c	4.4×10^{-4}	4.4×10^{-4}	4.4×10^{-4}	4.3×10^{-4}	2.1×10^{-4}	2.3×10^{-5}	2.3×10^{-7}

Table 3
Stability study: investigation of the numerical stability regions in terms of values of the ratio $\Delta t/\Delta t_c$, with Δt_c given by (45), for different domain decompositions, collocation point numbers, and transverse wavenumbers

Estimates of the largest timestep for stability: $\Delta t_{\max}/\Delta t_c$ in	Decomposition	Resolution	$k_\perp$
[1.8, 1.9]	$[0,1]$	1×40	1
[1.6, 1.7]	$[0,1]$	1×40	10^3
[1.2, 1.3]	$[0,1]$	1×40	10^4
[1.2, 1.3]	$[0,1]$	1×40	10^5
[1.8, 1.9]	$[0,1]$	1×80	1
[1.8, 1.9]	$[0,1]$	1×80	10^3
[1.3, 1.4]	$[0,1]$	1×80	10^4
[1.2, 1.3]	$[0,1]$	1×80	10^5
[1.8, 1.9]	$[0,\frac{1}{2}] \cup [\frac{1}{2},1]$	2×40	1
[1.1, 1.2]	$[0,\frac{1}{2}] \cup [\frac{1}{2},1]$	2×40	10^3
[1.2, 1.3]	$[0,\frac{1}{2}] \cup [\frac{1}{2},1]$	2×40	10^4
[1.2, 1.3]	$[0,\frac{1}{2}] \cup [\frac{1}{2},1]$	2×40	10^5
[1.8, 1.9]	$[0,\frac{1}{2}] \cup [\frac{1}{2},1]$	30 + 50	1
[1.7, 1.8]	$[0,\frac{1}{2}] \cup [\frac{1}{2},1]$	30 + 50	10^3
[1.2, 1.3]	$[0,\frac{1}{2}] \cup [\frac{1}{2},1]$	30 + 50	10^4
[1.8, 1.9]	$[0,\frac{1}{3}] \cup [\frac{1}{3},1]$	2×40	1
[1.5, 1.6]	$[0,\frac{1}{3}] \cup [\frac{1}{3},1]$	2×40	10^3
[1.2, 1.3]	$[0,\frac{1}{3}] \cup [\frac{1}{3},1]$	2×40	10^4
[1.8, 1.9]	$[0,\frac{1}{2}] \cup [\frac{1}{2},1]$	40 + 120	1
[1.8, 1.9]	$[0,\frac{1}{2}] \cup [\frac{1}{2},1]$	40 + 120	10^3
[1.7, 1.8]	$[0,\frac{1}{2}] \cup [\frac{1}{2},1]$	40 + 120	10^4
[1.2, 1.3]	$[0,\frac{1}{2}] \cup [\frac{1}{2},1]$	40 + 120	10^5

5.1. Acoustic plane waves of arbitrary wavenumbers in the m-variable

We consider the steady mean flow (46) in the m-variable. For an acoustic mode, the perturbed flow is isentropic. Consequently the pressure is proportional to the density, so that Eq. (7a) is equivalent to Eq. (7d). The perturbed flow is also irrotational, implying an algebraic relation between Eqs. (7b) and (7c). System (8) then reduces to two equations, which can be combined to give a single second-order hyperbolic equation satisfied by the four quantities, a specific form of the wave equation,

$$\left[\frac{\partial^2}{\partial t^2} - \left(\bar{\rho}\bar{c}\right)^2 \frac{\partial^2}{\partial m^2} + \left(k_\perp \bar{c}\right)^2\right]\mathbf{V} = 0, \tag{47}$$

with $\mathbf{V} = (\rho \quad v_x \quad \nabla_\perp \cdot \vec{v}_\perp \quad p)^{\mathsf{T}}$. We consider periodic boundary conditions in which case a particular solution is given by plane acoustic waves of the form

$$g(m,t) = \mathscr{A} \sin\left(k_m m - \omega t\right), \tag{48}$$

where the pulsation $\omega = 2\pi/T$, T denoting the period of the wave, is given by $\omega = \bar{c}\sqrt{(\bar{\rho}k_m)^2 + k_\perp^2}$, and $\mathscr{A}$ is the plane wave amplitude. A corresponding solution $\mathbf{V}$ of (8) is

$$\begin{aligned}
&\rho(m,k_\perp,t) = \bar{\rho} g(m,t),\\
&v_x(m,k_\perp,t) = \bar{c}^2 \frac{\bar{\rho} k_m}{\omega} g(m,t),\\
&\nabla_\perp \cdot \vec{v}_\perp(m,k_\perp,t) = \bar{c}^2 \frac{k_\perp^2}{k_m \omega} \frac{\partial g}{\partial m}(m,t),\\
&p(m,k_\perp,t) = \bar{c}^2 \rho.
\end{aligned} \tag{49}$$

Computations of these particular modes are carried out with 40 collocation points per subdomain and a critical timestep computed from (44). Several values of $k_\perp$ are considered in the range $[1, 10^4]$. Let us recall that for fixed k_m – here taken to be $k_m = 2\pi$ – increasing values of $k_\perp$ correspond to larger propagation angles of the plane wave with respect to the x-axis. The variation of the critical timestep with respect to the transverse wavenumber $k_\perp$ is summarized in Table 2. These results show that for $k_\perp \ll (N-1)^2$, the timestep is driven by the CFL condition for the one-dimensional – i.e., purely longitudinal – system, where Δt_c classically behaves like $(N-1)^{-2}$. On the contrary, for $k_\perp \gg (N-1)^2$ the critical timestep behavior is dominated by $k_\perp$, namely as $\Delta t_c \sim k_\perp^{-1}$. Computed density profiles are displayed in Fig. 2, for wavenumbers $k_m = 2\pi$ and $k_\perp = 10$ and at four different times. From this figure, one can notice that this single acoustic plane wave is well reproduced for times up to a period.

This tendency is confirmed by relative error plots given in Fig. 3(a) for time running between 1 and 100 periods. However a linear growth of this error is clearly seen in this figure. Nevertheless the levels

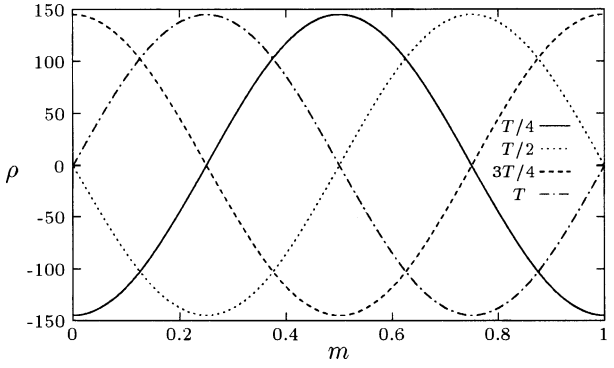

Fig. 2. Acoustic plane waves of arbitrary wavenumbers. Density profiles, for 2×40 collocation points, for wavenumbers $k_m = 2\pi$ and $k_\perp = 10$, at four different times $t = T/4, T/2, 3T/4, T$, where T is the plane wave period.

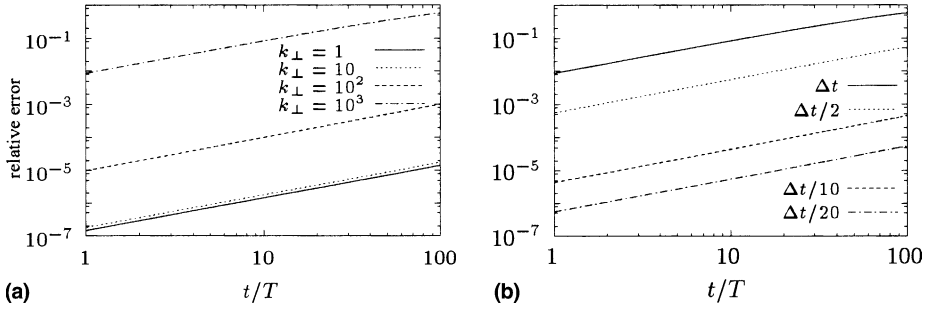

Fig. 3. Acoustic plane waves of arbitrary wavenumbers. (a) Largest relative errors upon the density vs. the number of periods, for 2×40 collocation points, for wavenumbers $k_m = 2\pi$ and $k_\perp = 1, 10, 100, 1000$. (b) Same as in (a), but the transverse wavenumber is kept fixed at $k_\perp = 1000$. The timestep is divided by 2, 10 and 20, respectively.

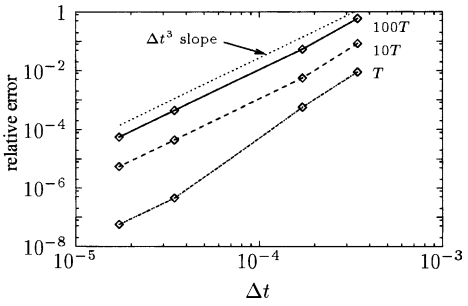

Fig. 4. Acoustic plane waves of arbitrary wavenumbers. Relative error profiles upon the density vs. the timestep, for 2×40 collocation points, wavenumbers $k_m = 2\pi$ and $k_\perp = 1000$, at three different times $t = T, 10T, 100T$, where T is the plane wave period.

of these errors confirm that the scheme is used in its stability region. Indeed computations performed with a sufficiently large Δt are clearly unstable. We notice (Fig. 3(a)) that the error level, which is relatively small for $k_\perp = 1$ or 10, over the full time range, increases with $k_\perp$. These larger errors are explained by the fact that the critical timestep is driven by the stability condition and not by any accuracy requirement. Indeed, computations over a period, for $k_\perp = 1$ or 10, represent about 700 cycles of the scheme, while for $k_\perp = 1000$ a full period is covered in only 20 cycles. Consequently one can expect poorer resolution in this case. In order to check this point, we performed computations where the timestep was divided by 2, 10 and 20 corresponding, respectively, to 40, 200, 400 cycles per period: see Fig. 3(b). The error level obviously decreases with diminishing timesteps. For example, a calculation with $k_\perp = 100$ and a timestep Δt_c given by (44), and a second calculation with $k_\perp = 1000$ and a timestep equal to 1/10 of the value given by (44) lead to the same number of cycles per period and comparable errors (compare Fig. 3(a) and (b)).

Relative errors versus timestep values (curves in Fig. 4) evidence a Δt^3 behavior, thus confirming that the time integration scheme is third-order accurate. Spatial density error profiles are shown in Fig. 5, for the two values of $k_\perp = 1$ and 100 at three different times. These errors appear to be minimal near the zeroes of the solution and maximum about the solution extrema. Note that the location of the zeroes of the computed densities do not evolve from period to period, even after 100 periods. This indicates that the numerical errors are amplitude errors rather than phase errors. In addition these results show that the periodic boundary conditions and matching condition are correctly handled.

From these computations, it appears that the critical timestep values given by (44) ensure the use of the numerical scheme in its stability region. However this timestep determination does not obviously guaranty error levels which are uniform with respect to the angle of propagation (here identified by $k_\perp$) of acoustic plane waves.

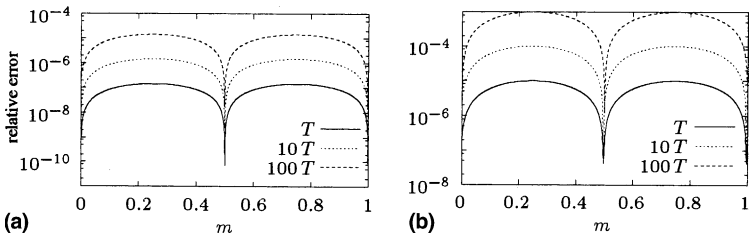

Fig. 5. Acoustic plane waves of arbitrary wavenumbers. Relative error profiles upon the density, for 2×40 collocation points, for wavenumbers $k_m = 2\pi$ and $k_\perp = 1$ (a) and $k_\perp = 100$ (b), at three different times $t = T, 10T, 100T$, where T is the plane wave period.

5.2. Vorticity mode in the m-variable

Here again we use the steady mean flow (46) in the m-variable. In the linear approximation, vorticity modes are characterized by perturbations of entropy, pressure and divergence of the velocity field which are zero [2]. This corresponds to steady solenoidal velocity fields. With the retained coordinate system (m, y, z), such vorticity modes are stationary. As a particular case, we choose the x-component of the velocity field to be (see Fig. 6)

$$v_x(m, k_\perp, t) = \begin{cases} \exp\left[\left(\frac{m-\mu_0}{\mu_1-\mu_0}\right)^2\left(\frac{m-\mu_1}{\mu_1-\mu_0}\right)^2\right] - 1 & \text{for } m \in [\mu_0, \mu_1], \\ 0 & \text{elsewhere.} \end{cases} \tag{50}$$

In this definition, μ_0 and μ_1 can be chosen arbitrarily within the computational domain. The transverse expansion $\nabla_\perp \cdot \vec{v}_\perp$ is deduced from the constraint that the velocity field should be solenoidal, i.e.,

$$\nabla \cdot \vec{v} = \bar{\rho}\frac{\partial v_x}{\partial m} + \nabla_\perp \cdot \vec{v}_\perp = 0. \tag{51}$$

The non-zero component of the vorticity is then

$$\overrightarrow{\mathrm{rot}}\,\vec{v} \cdot \overrightarrow{e_z} = -\mathrm{i}k_\perp\left(\frac{\bar{\rho}}{k_\perp^2}\frac{\partial}{\partial m}\nabla_\perp \cdot \vec{v}_\perp + v_x\right) \tag{52}$$

taking $k_z = 0$. Boundary conditions in this case are taken to be of the non-reflecting type.

As a result, the critical timestep is evaluated with Eq. (45). This timestep variation versus $k_\perp$ is reproduced in Fig. 7. We present in Fig. 8 the value of the divergence of the velocity for four different resolutions, at time $t = 10$, $k_\perp = 10$ and for the particular choice $\mu_0 = 0.5$ and $\mu_1 = 1$ in (50). These results show that the computed solution remains solenoidal. Note that due to the particular definition (50), the transverse expansion is of class $\mathscr{C}^0([0, 1])$ in which case one can expect numerical errors at the edges μ_0 and μ_1 to be larger than for the rest of the domain. This is indeed the case as seen in Fig. 8. Apart from this feature, the numerical errors indicate that the non-reflecting boundary treatment behaves correctly here.

5.2.1. Stability study

We check the stability analysis performed in Section 4 by investigating the maximum timestep values for stability, $\Delta t_{\max}$, in a series of numerical computations performed for different domain decompositions, numbers of collocation points, and transverse wavenumbers. From this study, it turns out that (see Table 3):

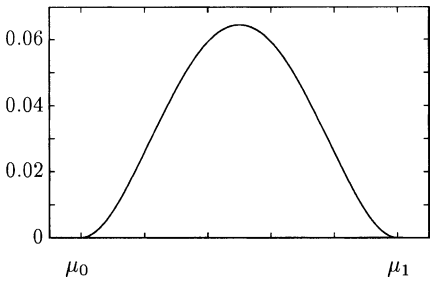

Fig. 6. Vorticity mode. Initial perturbation defined from Eq. (50).

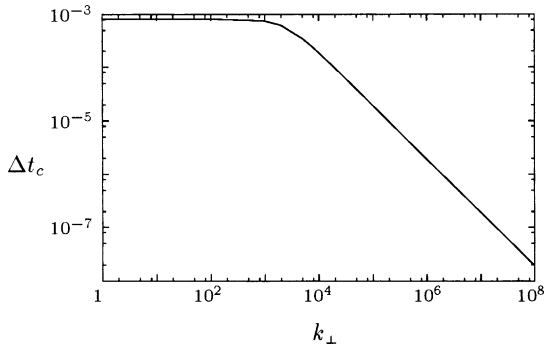

Fig. 7. Vorticity mode. Critical timestep vs. the transverse wavenumber, in the case of 2×40 collocation points, and Dirichlet boundary conditions.

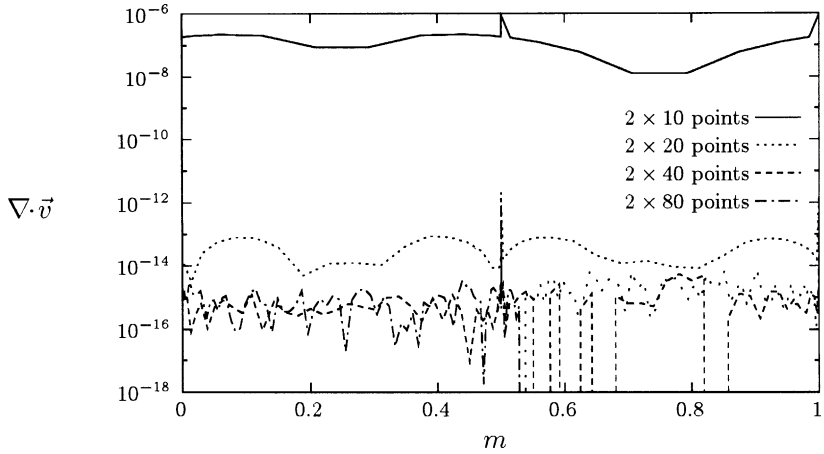

Fig. 8. Vorticity mode. Velocity divergence, for four different spatial resolutions, for transverse wavenumber $k_\perp = 10$ at time $t = 10$.

1. The stability condition $\Delta t \leqslant \Delta t_c$ (45) appears to be a sufficient condition for stability, for all decompositions, numbers of collocation points and transverse wavenumbers tested.
2. For small values of $k_\perp$, Δt_c is clearly below $\Delta t_{\max}$ whatever the number of collocation points used. As already noted from Table 2 and Fig. 7, the behavior of Δt_c is then dominated by the dependence in $(N-1)^{-2}$.
3. For large values of $k_\perp$, Δt_c is close to $\Delta t_{\max}$. Therefore, $\Delta t_{\max}$ evolves as $k_\perp^{-1}$.
4. The ratio $\Delta t_{\max}/\Delta t_c$ is most sensitive to spatial resolution and domain decomposition for intermediate values of $k_\perp$, where $k_\perp \simeq (N-1)^2$.

5.3. Entropy mode in the ξ-variable

For the mean flow of Sections 5.1 and 5.2, we now choose to solve the perturbation equations in their (ξ, t)-variable formulation (Eqs. (A.6)–(A.8), Appendix A) for $\alpha = 1$. Consequently the coefficients of the PDEs are no longer constant in time nor uniform in space (cf. Appendix A). In other words, the situation is equivalent to solving numerically these PDEs for a non-constant and non-uniform mean flow.

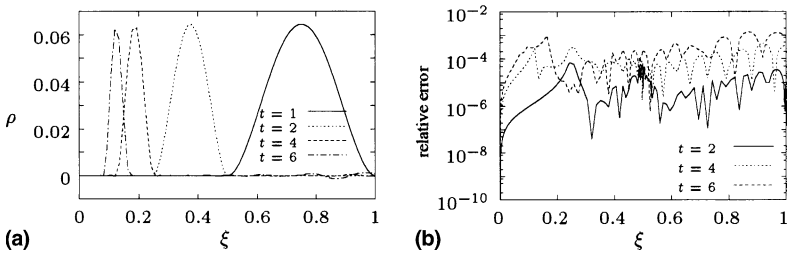

Fig. 9. Entropy mode. Density profiles (a) and relative errors (b), for 2×50 collocation points, at four different times.

Entropy modes are characterized by zero pressure and velocity perturbations [2], so that the acoustic and vorticity modes are also zero. Any initial density perturbation satisfying a zero pressure perturbation will comply with this definition for all times in the coordinate system (m, y, z). In the ξ-coordinate system, an entropy mode undergoes a non-uniform translation and shrinks as time goes on.

Choosing the computational domain to be $0 \leqslant \xi \leqslant 1$ with two subdomains defined as in the beginning of Section 5, we consider computations for time $t \geqslant t_0 > 0$ and non-reflecting boundary conditions at both ends of the domain. The density perturbation, including its initial condition, is chosen to be given by the function

$$\rho(\xi, k_\perp, t) = \begin{cases} \exp\left[\left(\frac{\xi t/t_0 - \Xi_0}{\Xi_1 - \Xi_0}\right)^2 \left(\frac{\xi t/t_0 - \Xi_1}{\Xi_1 - \Xi_0}\right)^2\right] - 1, & \xi \in \left[\Xi_0 \frac{t_0}{t}, \Xi_1 \frac{t_0}{t}\right] \\ 0, & \xi \in \left[0, \Xi_0 \frac{t_0}{t}\right] \cup \left[\Xi_1 \frac{t_0}{t}, 1\right] \end{cases} \tag{53}$$

for $t \geqslant t_0$.

The timestep constraint is then estimated with (45), but for which the eigenvalues of the corresponding discretized operator $\mathbf{S}_{4N}$ (Eq. (24)) are taken to be $(\lambda - \xi)/t$ where λ stands for the eigenvalues of $\mathbf{S}_{4N}$ in the (m, t)-formulation (cf. Appendix A, Eq. (A.9)).

Results of computations for the particular case $\Xi_0 = 0.5, \Xi_1 = 1, t_0 = 1$ with 50 collocation points per subdomain are shown in Fig. 9. Density profiles (Fig. 9(a)) at different times clearly illustrate the non-uniform convection and contraction of the entropy mode. As a result of this contraction, the non-zero portion of the solution is described by fewer and fewer points as time increases. Starting with 50 points for the initial density profile, the spatial representation only uses eight points to approximate the same profile at time $t = 6$. As a consequence, the error deteriorates with increasing time as one can notice on Fig. 9(b) and near the right end of the computational domain for $t = 6$ (see Fig. 9(a)). A remedy for this shortcoming would be of course to use dynamical adaptive techniques for determining the sub-domain boundary location and optimizing the coordinate mapping within each subdomain, e.g. see [8,19].

5.4. Forced longitudinal acoustic mode in the m- and ξ-variables

As a final test, we consider the excitation of a longitudinal acoustic plane wave ($k_\perp = 0$) by means of a time-dependent density law imposed at one of the boundaries of the computational domain, for the same uniform mean flow (46). We choose to solve this problem in both the m- and ξ-coordinate systems for $\alpha = 1$. In each case, the imposed time-dependent density boundary condition is chosen to be applied at the left boundary ($m = 0$ or $\xi = 0$), while the boundary condition at the right boundary ($m = 1$ or $\xi = (t_0 + T)^{-1}$) is taken to be of the non-reflecting type. More precisely, the physical boundary condition for the perturbed density follows the law

$$\rho_0(t) = \bar{\rho} g(m = 0, t), \tag{54}$$

where $\omega = \bar{\rho}\bar{c}k_m$ and g is given by Eq. (48). For initial conditions $\mathbf{V}(m, k_\perp, t = 0) = 0$, the perturbed density solution is

$$\rho(m,t) = \begin{cases} \bar{\rho} g(m,t), & 0 \leqslant m \leqslant \bar{\rho}\bar{c}t, \\ 0 & \text{elsewhere}, \end{cases} \tag{55}$$

while other quantities evolve according to Eq. (49) with $k_\perp = 0$. The corresponding definitions of (54) and (55) in the ξ-variable are readily obtained from the transformation (5) for $t \geqslant t_0 > 0$. The treatment of the imposed density boundary condition follows from Eq. (21).

5.4.1. Solution in the m-variable

Numerical computations are performed with a timestep such that $\Delta t \leqslant \Delta t_c$, with (45). Spatial density profiles for times $t = T/4, T/2, 3T/4, T$ (Fig. 10(a)) show the acoustic wave front entering at the domain left boundary and propagating until it starts exiting at the opposite boundary. Largest relative numerical errors in terms of density are also shown in Fig. 10(b) for time between $T/100$ and $100T$. These errors – plotted in log–log scales – are characterized by a rather high level ($\simeq 10^{-1}$) for the whole duration of the wave front propagation inside the domain, i.e., for $0 \leqslant t \leqslant T$. This behavior is due to the fact that the solution (55) is only $\mathscr{C}^0$ at the wave front. Indeed as time increases beyond one period, the error significantly decreases and reaches a plateau below 10^{-5} for $t \geqslant 2T$. In particular, this result illustrates a proper implementation of a particular case of time-dependent boundary conditions and of a non-reflecting boundary condition at a characteristic boundary ($m = 1$).

5.4.2. Solution in the ξ-variable

Here the critical timestep is evaluated as described in Section 5.3. The equivalent of Fig. 10 (density profiles and relative errors) is reproduced in Fig. 11 for this situation, where now $t \geqslant t_0 = 1$. The behavior of the density profiles (Fig. 11(a)) is similar to the previous case for $0 \leqslant t \leqslant T$. For $t - t_0 \geqslant T$, the wave front leaves the domain through the non-reflecting boundary and the acoustic wave keeps propagating while undergoing the non-uniform contraction due to the transformation $m \to \xi$. As a result, more and more oscillations accumulate near the left boundary ($\xi = 0$). As a consequence, the numerical errors tend to grow as time increases due to the deterioration of the spatial resolution in this region. This behavior is illustrated on Fig. 11(b) for $t - t_0 \geqslant 2T$ by the positive slope of the error curve.

In addition, we have studied the accuracy of the time-integration scheme in this case of a non-uniform time-dependent mean flow and of a time-dependent boundary condition. For this purpose, computations have been carried out for values of the timestep ranging from 4×10^{-5}–10^{-3}. The absolute errors, obtained

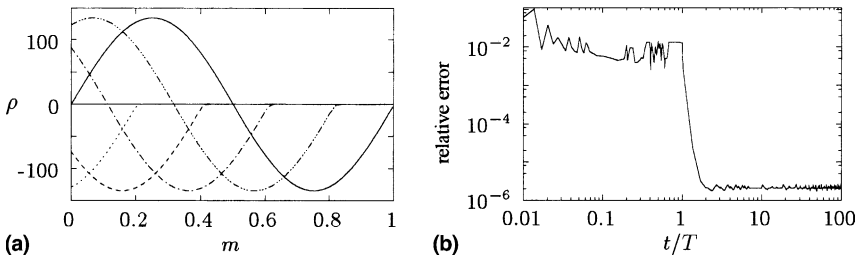

Fig. 10. Forced longitudinal acoustic mode in the m-variable. Density profiles (a) at $t = T/4, T/2, 3T/4, T$ (from left to right), for 2×40 collocation points. Largest relative error (b) vs. the number of periods.

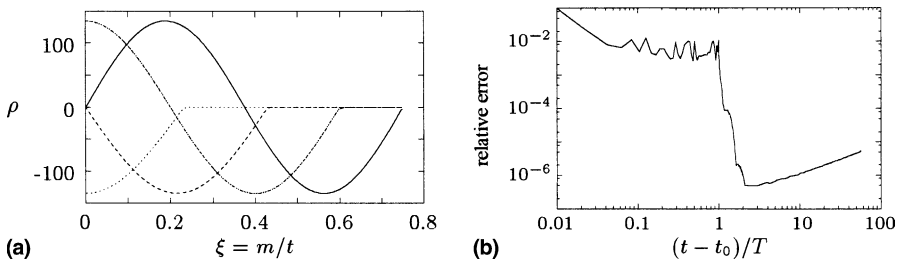

Fig. 11. Forced longitudinal acoustic mode in the ξ-variable. Density profiles (a) at $t - t_0 = T/4, T/2, 3T/4, T$ (from left to right), for 2×40 collocation points. Largest relative error (b) vs. the number of periods.

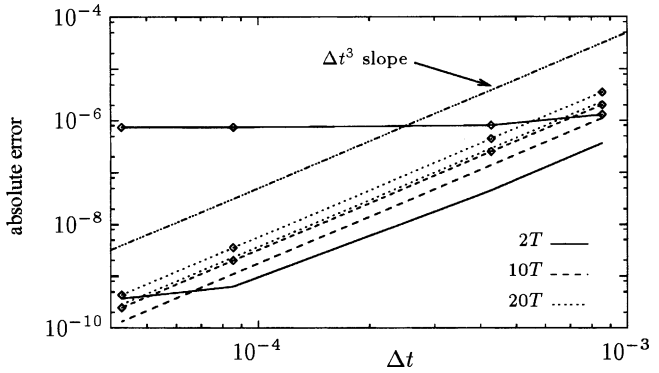

Fig. 12. Forced longitudinal acoustic mode in the ξ-variable. Absolute error profiles upon the density vs. the timestep, (lines: domain interiors; lines with symbols: domain boundaries) for 2×40 collocation points, for wavenumbers $k_m = 2\pi$ and $k_\perp = 0$ at three different times $t - t_0 = 2T, 10T, 20T$, where T is the plane wave period.

at different times ($(t - t_0)/T = 2, 10, 20$), clearly show that the Δt^3 dependence is recovered both within the domains and at the boundaries for $t - t_0 > 2T$ (see Fig. 12). Indeed, for $t - t_0 = 2T$, the errors result from the fact that the solution is only $\mathscr{C}^0$ in space for $t - t_0 \leqslant T$.

6. Conclusion

We have developed a pseudo-spectral method for handling one-dimensional systems of PDEs which arise from linearizing the Euler equations about an exact solution depending eventually on space and time. Our approach is based on a Fourier analysis of the transverse perturbed motion. As a result the transverse wavenumber $k_\perp$ is involved in the linear perturbation differential system and deeply influences its properties. The present numerical method utilizes two subdomains with a Chebyshev discretization and an explicit three-step third-order Runge–Kutta scheme. Treatments of physical boundary conditions and matching conditions are handled following the approaches suggested by Thompson [22,23] and Kopriva [10]. An analytical stability analysis of the numerical method is performed for any explicit three-step third-order non-degenerate Runge–Kutta scheme, which may be applied to several types of spatial discretization (Fourier, Chebyshev or finite-differences) provided that the first-order spatial derivative operator can be put in diagonal form. This analysis, carried out for a uniform mean flow over a single computational domain, emphasizes the role of the transverse wavenumber.

Numerical experiments show that this constraint may be used on two-subdomain configurations provided the minimum of the two subdomain constraints is retained. Four series of test cases have been carried out for the three basic fluctuation modes of a compressible flow: acoustic, vorticity and entropy modes. Acoustic plane waves of arbitrary wavenumbers (Section 5.1), solved with a steady mean flow and periodic boundary conditions, confirm that the time integration scheme is third-order accurate. However the amplitude error grows linearly with time and is larger as the angle of propagation increases. Vorticity mode computations (Section 5.2), carried out for a steady mean flow and non-reflecting boundary conditions, show that our current treatment of non-reflecting boundaries behaves correctly for this kind of non-propagating modes with non-zero transverse wavenumber. In addition, these computations have been used to check the numerical stability criterion we propose. Computations of an entropy mode (Section 5.3) for a time-dependent mean flow and non-reflecting boundary conditions display satisfactory error levels and expected behaviors. Finally a longitudinal acoustic plane wave excited by a time-dependent boundary condition (Section 5.4) has been computed for both a time independent and a time-dependent mean flow. The former configuration illustrates proper treatments of a time-dependent boundary condition and of a non-reflecting boundary condition at a characteristic boundary. The latter configuration confirms that the absolute errors behave as Δt^3 both within the subdomains and at the boundaries, for a time-dependent mean flow and a time-dependent boundary condition.

More generally, we have shown that the accuracy of the method is governed by the timestep and not by the transverse wavenumber $k_\perp$. As a consequence, achieving a given level of accuracy may require smaller timestep values than those imposed by the numerical stability constraint. In that respect, the advantage of using a time implicit scheme appears here to be marginal. The present method may be improved by using a multidomain or a dynamical multidomain approach. Applications of this method to some situations of physical interest will be given in forthcoming papers.

Appendix A. Derivation of linear perturbation equations

The system of equations satisfied by the linear perturbations is derived from (1) in the following manner.

We first perform in (1) the change of variables $\vec{x} \to \vec{X} = (m, y, z)$ with m defined by (2). By making use of the partial derivative transformations

$$\frac{\partial}{\partial x} \to \bar{\rho}\frac{\partial}{\partial m} \quad \text{and} \quad \frac{\partial}{\partial t} \to \frac{\partial}{\partial t} - \bar{\rho}\bar{v}_x\frac{\partial}{\partial m},$$

the equations of motion in the new variables follow as

$$\begin{aligned}
&\frac{\partial \rho}{\partial t} + \bar{\rho}(v_x - \bar{v}_x)\frac{\partial \rho}{\partial m} + \vec{v}_\perp \cdot \nabla_\perp \rho + \rho\left(\bar{\rho}\frac{\partial v_x}{\partial m} + \nabla_\perp \cdot \vec{v}_\perp\right) = 0,\\
&\rho\left(\frac{\partial v_x}{\partial t} + \bar{\rho}(v_x - \bar{v}_x)\frac{\partial v_x}{\partial m} + \vec{v}_\perp \cdot \nabla_\perp v_x\right) + \bar{\rho}\frac{\partial p}{\partial m} = 0,\\
&\rho\left(\frac{\partial \vec{v}_\perp}{\partial t} + \bar{\rho}(v_x - \bar{v}_x)\frac{\partial \vec{v}_\perp}{\partial m} + \vec{v}_\perp \cdot \nabla_\perp \vec{v}_\perp\right) + \nabla_\perp p = \vec{0},\\
&\frac{\partial p}{\partial t} + \bar{\rho}(v_x - \bar{v}_x)\frac{\partial p}{\partial m} + \vec{v}_\perp \cdot \nabla_\perp p + \gamma p\left(\bar{\rho}\frac{\partial v_x}{\partial m} + \nabla_\perp \cdot \vec{v}_\perp\right) = 0,
\end{aligned} \tag{A.1}$$

with the notations $\vec{v}_\perp = v_y\vec{e}_y + v_z\vec{e}_z$, $\nabla_\perp = (\partial/\partial y \quad \partial/\partial z)^{\mathrm{T}}$ for the *transverse* velocity field and transverse gradient operator, all quantities being now taken as functions of $\vec{X}$ and t.

We then assume that all the flow quantities depend on a perturbation parameter, say ε, such that $\varepsilon = 0$ corresponds to the mean flow, i.e., $\varphi(\vec{X}, t; \varepsilon)|_{\varepsilon=0} \equiv \bar{\varphi}(m, t)$ for any scalar quantity φ. By defining the linear perturbation of φ to be the partial derivative

$$\varphi'(\vec{X}, t) = \left.\frac{\partial \varphi}{\partial \varepsilon}(\vec{X}, t; \varepsilon)\right|_{\varepsilon=0}, \tag{A.2}$$

the equations satisfied by $\rho', \vec{v}', p'$ are obtained formally by differentiating, with respect to ε, the equations in (A.1), keeping in mind that $\vec{X}, t, \varepsilon$ are taken as *independent variables*. This definition corresponds to an Eulerian description of the perturbations (e.g. see [16], Section 56) in the coordinate system (m, y, z). The resulting system – a particular form of the linearized Euler equations – reads

$$\frac{\partial \rho'}{\partial t} + \bar{\rho}^2 \frac{\partial v_x'}{\partial m} + \bar{\rho}\left(\frac{\partial \bar{v}_x}{\partial m}\rho' + \frac{\partial \bar{\rho}}{\partial m} v_x' + \nabla_\perp \cdot \vec{v}_\perp'\right) = 0, \tag{A.3a}$$

$$\frac{\partial v_x'}{\partial t} + \frac{\partial p'}{\partial m} - \frac{1}{\bar{\rho}}\frac{\partial \bar{p}}{\partial m}\rho' + \bar{\rho}\frac{\partial \bar{v}_x}{\partial m} v_x' = 0, \tag{A.3b}$$

$$\frac{\partial \vec{v}_\perp'}{\partial t} + \frac{1}{\bar{\rho}}\nabla_\perp p' = \vec{0}, \tag{A.3c}$$

$$\frac{\partial p'}{\partial t} + \gamma \bar{p}\left(\bar{\rho}\frac{\partial v_x'}{\partial m} + \nabla_\perp \cdot \vec{v}_\perp'\right) + \bar{\rho}\left(\frac{\partial \bar{p}}{\partial m} v_x' + \gamma \frac{\partial \bar{v}_x}{\partial m} p'\right) = 0, \tag{A.3d}$$

where (A.3b) is derived with the help of the equation for $\bar{v}_x$ in (3).

As is usual, two major simplifications of the above system of equations can be carried out. One may indeed replace, in the above system of equations, the unknown $\vec{v}_\perp'$ by its divergence $\nabla_\perp \cdot \vec{v}_\perp'$ – called here transverse *expansion*. Taking the transverse divergence of (A.3c) yields then the evolution equation for this new unknown. Another equation, accounting for the evolution of solenoidal transverse motions, should in principle be added at this point. However such motions are time independent and hence are solid rotations about Ox with angular velocities stipulated by initial conditions.

The second simplification consists in considering the Fourier transforms, in the y- and z-variables, of the equations. The resulting system is then simply given by (A.3a), (A.3b), and (A.3d) along with

$$\frac{\partial}{\partial t}\left(\nabla_\perp \cdot \vec{v}_\perp'\right) - \frac{k_\perp^2}{\bar{\rho}} p' = 0, \quad \text{where} \quad k_\perp = \sqrt{k_y^2 + k_z^2}, \tag{A.4}$$

with the convention that φ', for any φ, stands now for the Fourier transform of the corresponding linear perturbation. Consequently φ' is a complex-valued function of the variables m, k_y, k_z – the Fourier space variables, i.e., the y- and z-wavenumbers – and t. However as these wavenumbers only appear explicitly in (A.4) through the *transverse wavenumber* $k_\perp$, φ' may be considered as a function of $(m, k_\perp, t)$ only. Different values of (k_y, k_z) are then distinguished by the corresponding initial and boundary condition Fourier transforms.

We note that assuming two-dimensional motions for the linear perturbations yields an equivalent formulation for the Fourier transformed equations.

A.1. Formulation in the self-similar variable ξ

For self-similar mean flows of the form (4), it is convenient to proceed to the change of variable $m \to \xi$ in (A.3a), (A.3b), (A.3d), and (A.4). We do so by introducing non-dimensional wavenumber and time variables, $\kappa_\perp$ and t_*, according to the relations

$$\kappa_\perp = \ell k_\perp, \quad t_* = t/\tau, \tag{A.5}$$

where ℓ is a length scale to be chosen and τ the associated time scale, $\tau = (\varrho\ell/A)^{1/\alpha}$.

We then define non-dimensional linear perturbations $G, V_x, \nabla_\perp \cdot V, P$ to be the functions of $(\xi, \kappa_\perp, t_*)$ given by the relations

$$\rho' = \varrho G, \quad v_x' = \frac{A}{\varrho}\tau^{\alpha-1}V_x, \quad \nabla_\perp \cdot \vec{v}_\perp' = \tau^{-1}\nabla_\perp \cdot V, \quad p' = \frac{A^2}{\varrho}\tau^{2(\alpha-1)}P.$$

Using these definitions in conjunction with the similarity transformation (4) and (5) leads to replacing (A.3a), (A.3b), (A.3d), and (A.4) by the equation

$$\frac{\partial \mathbf{V}_*}{\partial t_*} + \mathbf{A}_* \frac{\partial \mathbf{V}_*}{\partial \xi} + \mathbf{B}_* \mathbf{V}_* = \mathbf{0}, \tag{A.6}$$

with $\mathbf{V}_* = (G\ V_x\ \nabla_\perp \cdot V\ P)^{\mathsf{T}}$,

$$\mathbf{A}_* = \begin{pmatrix} -\alpha\xi/t_* & \bar{G}^2/t_*^\alpha & 0 & 0 \\ 0 & -\alpha\xi/t_* & 0 & 1/t_*^\alpha \\ 0 & 0 & -\alpha\xi/t_* & 0 \\ 0 & t_*^{\alpha-2}\left(\bar{G}\bar{C}\right)^2 & 0 & -\alpha\xi/t_* \end{pmatrix}, \tag{A.7}$$

where $\bar{C}$ denotes the reduced function for the isentropic sound velocity, i.e., $\bar{C} = \sqrt{\gamma\bar{P}/\bar{G}}$, and

$$\mathbf{B}_* = \begin{pmatrix} \frac{\bar{G}}{t_*}\frac{\mathrm{d}\bar{V}}{\mathrm{d}\xi} & \frac{\bar{G}}{t_*^\alpha}\frac{\mathrm{d}\bar{G}}{\mathrm{d}\xi} & \bar{G} & 0 \\ -\frac{t_*^{\alpha-2}}{\bar{G}}\frac{\mathrm{d}\bar{P}}{\mathrm{d}\xi} & \frac{\bar{G}}{t_*}\frac{\mathrm{d}\bar{V}}{\mathrm{d}\xi} & 0 & 0 \\ 0 & 0 & 0 & -\frac{\kappa_\perp^2}{\bar{G}} \\ 0 & t_*^{\alpha-2}\bar{G}\frac{\mathrm{d}\bar{P}}{\mathrm{d}\xi} & \gamma t_*^{2\alpha-2}\bar{P} & \gamma\frac{\bar{G}}{t_*}\frac{\mathrm{d}\bar{V}}{\mathrm{d}\xi} \end{pmatrix}. \tag{A.8}$$

We note that the two systems of Eqs. (7a)–(7d) – or equivalently (8) – and (A.6) are of identical forms. Furthermore, system (A.6) is, like (8), nonstrictly hyperbolic, the spectrum of $\mathbf{A}_*$ being deduced from that of the matrix $\mathbf{A}$ of (9) via the transformation

$$\Lambda^i \mapsto \Lambda^i/t_*^\alpha - \alpha\xi/t_*, \tag{A.9}$$

while the associated eigenvectors are those of (12) but expressed in terms of the reduced functions $\bar{G}$, $\bar{C}$, and of t_*. However, unlike the matrix $\mathbf{A}$, $\mathbf{A}_*$ is neither constant in time nor uniform in space as soon as the similarity exponent α in (5) is non-zero.

Appendix B. A linear algebra theorem

Theorem B.1. *Let* $\mathbf{M}$ *be a* $2N \times 2N$ *matrix of the form*

$$\mathbf{M}_{2N} = \begin{pmatrix} \zeta_1\mathbf{I}_N & \mathbf{\Psi}^U \\ \mathbf{\Psi}^L & \zeta_2\mathbf{I}_N \end{pmatrix}, \tag{B.1}$$

where $\mathbf{\Psi}^{L,U} = \mathrm{diag}(\psi_j^{L,U})$, $j = 1, \ldots, N$, $\zeta_i \in \mathbb{R}$, $i = 1, 2$, *then*

$$\det \mathbf{M}_{2N} = \prod_{j=1}^{N} \left(\zeta_1 \zeta_2 - \psi_j^L \psi_j^U \right) \quad \forall N \geqslant 1.$$

Proof. The proof follows by induction on N. For $N = 1$, we have $\det \mathbf{M}_2 = \zeta_1 \zeta_2 - \psi_1^U \psi_1^L$. For $N > 1$, we compute $\det \mathbf{M}_{2N}$ in terms of $\det \mathbf{M}_{2(N-1)}$ as follows. $\det \mathbf{M}_{2N}$ reads

$$\det \mathbf{M}_{2N} = \begin{vmatrix} \zeta_1 & & & \psi_1^U & & & \\ & \ddots & & & \ddots & & \\ & & \zeta_1 & & & & \psi_N^U \\ \psi_1^L & & & \zeta_2 & & & \\ & \ddots & & & \ddots & & \\ & & \psi_N^L & & & & \zeta_2 \end{vmatrix}. \tag{B.2}$$

By means of the linear combination $\zeta_1 \times 2N\text{th row} - \psi_N^L \times N\text{th row}$, the $2N$th-row reduces to its diagonal coefficient. Expanding the resulting determinant with respect to this very row yields

$$\det \mathbf{M}_{2N} = \frac{1}{\zeta_1} \left(\zeta_1 \zeta_2 - \psi_N^U \psi_N^L \right) \begin{vmatrix} \zeta_1 & & & & & \psi_1^U & & \\ & \ddots & & & & & \ddots & \\ & & \zeta_1 & 0 & & & & \psi_{N-1}^U \\ 0 & \cdots & 0 & \zeta_1 & 0 & \cdots & 0 & \\ \psi_1^L & & & & \zeta_2 & & & \\ & \ddots & & & & & \ddots & \\ & & & \psi_{N-1}^L & 0 & & \zeta_2 & \end{vmatrix}. \tag{B.3}$$

The unexpanded determinant in this expression obviously evaluates to $\zeta_1 \det \mathbf{M}_{2(N-1)}$, so that we have

$$\det \mathbf{M}_{2N} = \left(\zeta_1 \zeta_2 - \psi_N^U \psi_N^L \right) \det \mathbf{M}_{2(N-1)}. \qquad \square \tag{B.4}$$

References

[1] D.L. Book, I.B. Bernstein, Fluid instabilities of a uniformly imploding ablatively driven shell, J. Plasma Phys. 23 (3) (1980) 521–533.

[2] B.T. Chu, L.S.G. Kovásznay, Non-linear interactions in a viscous heat-conducting compressible gas, J. Fluid Mech. 3 (1958) 494–514.

[3] P.G. Drazin, W.H. Reid, Hydrodynamic Stability, Cambridge University Press, New York, 1981.

[4] E. Godlewksi, P.-A. Raviart, Numerical Approximation of Hyperbolic Systems of Conservation Laws, Applied Mathematical Sciences, Springer, New York, 1996.

[5] D. Gottlieb, L. Lustman, E. Tadmor, Stability analysis of spectral methods for hyperbolic initial-boundary value systems, SIAM J. Numer. Anal. 24 (2) (1987) 241–256.

[6] D. Gottlieb, S.A. Orszag, Numerical Analysis of Spectral Methods: Theory and Application, CBMS Regional Conference Series in Applied Mathematics, vol. 26, SIAM, Philadelphia, 1977.

[7] D. Gottlieb, E. Tadmor, The CFL condition for spectral approximations to hyperbolic initial-boundary value problems, Math. Comput. 56 (194) (1991) 565–588.

[8] H. Guillard, J.-M. Malé, R. Peyret, Adaptive spectral methods with application to mixing layer computations, J. Comput. Phys. 102 (1) (1992) 114–127.

[9] C. Hirsch, Numerical computation of internal and external flows, Wiley, New York, 1991.

[10] D.A. Kopriva, A spectral multidomain method for the solution of hyperbolic systems, Appl. Numer. Math. 2 (1986) 221–241.

[11] D.A. Kopriva, Multidomain spectral solution of the Euler gas-dynamics equations, J. Comput. Phys. 96 (1991) 428–450.
[12] D.A. Kopriva, Multidomain spectral solution of compressible viscous flows, J. Comput. Phys. 115 (1994) 184–199.
[13] D.A. Kopriva, A conservative staggered-grid Chebyshev multidomain method for compressible flows. II. A semi-structured method, J. Comput. Phys. 128 (1996) 475–488.
[14] D.A. Kopriva, A staggered-grid multidomain spectral method for the compressible Navier–Stokes equations, J. Comput. Phys. 143 (1998) 125–158.
[15] D.A. Kopriva, J.H. Kolias, A conservative staggered-grid Chebyshev multidomain method for compressible flows, J. Comput. Phys. 125 (1996) 244–261.
[16] P. Ledoux, T. Walraven, Variable stars, in: Handbuch der Physik, Springer, New York, 1958, pp. 353–604.
[17] D.H. Munro, Rippled shock front solutions for testing hydrodynamic stability simulations, Phys. Fluids B 1 (1) (1989) 134–141.
[18] R. Peyret, Spectral methods for incompressible viscous flow, Springer, New York, 2002.
[19] F. Renaud, S. Gauthier, A dynamical pseudo-spectral domain decomposition technique: application to viscous compressible flows, J. Comput. Phys. 131 (1997) 89–108.
[20] J.-Ch. Robinet, J. Gressier, G. Casalis, J.-M. Moschetta, Shock wave instability and the carbuncle phenomenon: same intrinsic origin?, J. Fluid Mech. 417 (2000) 237–263.
[21] C.K.W. Tam, Advances in numerical boundary conditions for computational aeroacoustics, J. Comput. Acoustics 6 (4) (1998) 377–402.
[22] K. Thompson, Time dependent boundary conditions for hyperbolic systems, J. Comput. Phys. 68 (1987) 1–24.
[23] K. Thompson, Time-dependent boundary conditions for hyperbolic systems, II, J. Comput. Phys. 89 (1990) 439–461.
[24] N. Toqué, Contribution à l'étude d'instabilités d'interfaces en géométrie plane, cylindrique et sphérique, Thèse de doctorat, University of Paris VI, 1996.
[25] A. Velikovich, L. Phillips, Instability of a plane centered rarefaction wave, Phys. Fluids 8 (4) (1996) 1107–1118.
[26] J.H. Wilkinson, The algebraic eigenvalue problem, Oxford Science Publications, 1988.
[27] J.H. Williamson, Low-storage Runge–Kutta schemes, J. Comput. Phys. 35 (1) (1980) 48–56.
[28] J.G. Wouchuk, Growth rate of the linear Richtmyer–Meshkov instability when a shock is reflected, Phys. Rev. E 63 (056303) (2001) 1–13.
[29] Y. Yang, Q. Zhang, D.H. Sharp, Small amplitude theory of Richtmyer–Meshkov instability, Phys. Fluids 6 (5) (1994) 1856–1873.
[30] Ya.B. Zel'dovich, Yu.P. Raizer, Physics of shock waves and high-temperature hydrodynamic phenomena, Academic Press, New York, 1967.